AIAA SciTech Forum
8-12 January 2024, Orlando, FL
AIAA SCITECH 2024 Forum

10.2514/6.2024-1284

Mid-Deployment Model Switching of Tether-Net Systems for Active Debris Removal

Achira Boonrath*, Eleonora M. Botta†
University at Buffalo, Buffalo, New York, 14260

One of the most promising solutions to the issue of the increasing amount of space debris orbiting the Earth is net-based Active Debris Removal. For accurate contact detection of thin target geometries with lumped-parameter modeled nets in simulations, many nodes (possibly 10 or more) must be introduced along threads. However, such introduction significantly increases the computational cost of simulations. This work proposes a modeling approach that introduces additional nodes during the deployment phase of the simulation rather than at the beginning to reduce such costs. The approach conserves the net's total linear momentum and adheres to the work-energy principle when employed mid-simulation. Through both quantitative and qualitative comparisons of nets with and without model switching, this work demonstrates that the methodology does not alter the overall dynamics of the net flight toward the target in a significant way. Capture simulations of a scaled-down Envisat satellite model are performed, where the introduction of model switching results in approx. 2.45 times faster simulation without compromising accuracy in the representation of capture.

I. Introduction

The escalating quantity of debris in orbit around the Earth – particularly in Low Earth Orbit (LEO) – presents challenges to the safety of space missions; consequently, the need for technologies that can efficiently and safely remove orbital debris increases. The possibility of impact of large debris items (e.g., rocket upper stages and defunct satellites) with other objects is especially troubling, as numerous debris fragments can be generated and lead to catastrophic chain reactions of additional debris creation. An example of a collision in orbit occurred in 2009 when Cosmos 2251 and Iridium 33 collided, generating thousands of fragments [1].

Tether-net systems are considered promising among the proposed Active Debris Removal (ADR) technologies. The advantages of such systems include their lightweight nature, compact packaging inside a chaser spacecraft during rendezvous travel to the target debris, adaptability to the target's size and rotational state, and their ability to allow a safe distance to be maintained during the capture process [2–5]. Due to the technological readiness of tether-net systems for ADR applications being considered low-to-medium, it is crucial to analyze and understand the system's dynamics in space through simulation before proceeding with actual missions. As a result, simulators depicting the deployment and capture dynamics of tether nets in space have been developed by Benvenuto et al. [6], Medina et al. [7], Botta et al. [4, 8, 9], Shan et al. [10, 11], and Si et al. [12]. Recently, Zhang et al. [13] and Shan and Shi [14] introduced a simplified dynamics representation of the net meant to reduce the computational demands of the deployment phase of net simulations; however, the approximations made did not allow for the simulation for target capture.

Within simulations, the prevalent approach for modeling tether-net systems utilized the lumped-parameter model [4, 10, 15–19]. Of focus within this manuscript is the simulator developed by Botta et al. [4, 8, 9] based in Vortex Studio, a commercial multibody dynamics simulator developed by CM Labs Simulations Inc., available for research and educational purposes. The lumped-parameter model consolidates the mass of the physical net into small spherical rigid bodies, called *nodes*, which are connected via Kelvin-Voigt elements incapable of withstanding compression. Boonrath and Botta [20] demonstrated that additional nodes (referred to as *inner nodes*) are required to be appended along the threads of the net for capture of targets with thin geometries. However, this addition increases the computational cost by a large amount due to the increase in the degrees of freedom of the system. For example, in previous work by Boonrath and Botta [20], the simulation of lumped-parameter net deployment with no inner nodes is approx. 10 times faster to numerically integrate compared to the same scenario but with 20 inner nodes present. As such, this work proposes a methodology where inner nodes are added mid-simulation to decrease the computational cost involved in simulations that require inner nodes to be present for the capture phase. Adding inner nodes only before contact between the net and

*Ph.D. Student, Department of Mechanical and Aerospace Engineering, AIAA Student Member
†Assistant Professor, Mechanical and Aerospace Engineering, AIAA Senior Member

target will lower the computational cost of the deployment phase while preserving capture dynamics fidelity since inner nodes are not vital during the initial stages of net flight towards the target.

This paper will first discuss the net lumped-parameter modeling and the adherence requirements regarding linear impulse and momentum and work-energy principles in Section II. Section III then presents the model switching methodology, where the assignments of added inner knots and corner masses positions and velocities and the adjustment of stiffness and damping properties are discussed. Next, Section IV showcases the conservation of energy and momentum for nets with model switching occurring at different times, as well as quantitative and qualitative comparison of the geometrical shapes of the nets over time. Lastly, Section V concludes the manuscript with summary of the work.

II. Net Modeling and Conservation Requirements

A. Net Modeling

Multiple shapes, such as hexagonal, conical, and pyramidal, have been explored through simulation studies for nets intended for space debris capture [6, 13, 21–24]. However, one of the most common designs – used in this work– features a square-shaped net configuration with masses attached at each of the four corners [4, 6]. The square net itself is referred to as *net proper*, while the threads that link the corner masses to the net proper are called *corner threads*. Within Vortex Studio, the nodes are simulated as spherical rigid bodies connected by relaxed distance joints that only activate when the separation distance between adjacent nodes exceeds a specified length of an unstretched thread. The mass, denoted by m_i , aggregated in the i-th node, is determined as:

$$m_i = \begin{cases} \sum_{\xi \in \Xi_i} \frac{m_\xi}{2} + m_{knot} & 1 \leq i \leq N_s^2 \\ \sum_{\xi \in \Xi_i} \frac{m_\xi}{2} & i > N_s^2, i \notin I_{CM} \\ \sum_{\xi \in \Xi_i} \frac{m_\xi}{2} + m_{CM} & i \in I_{CM} \end{cases} \tag{1}$$

In the given equation m_ξ represent the mass of the thread sections neighboring the i-th node, belonging to set Ξ_i, N_s^2 is the total number of knots on the net proper, m_{knot} is the mass of a knot, located at a thread intersection, and m_{CM} is the mass of a corner element (for which index i belongs to the set I_{CM}). Inner nodes are given indices starting from $N_s^2 + 1$ to $N = N_s^2 + 2N_s(N_s - 1)N_I$, where N_I is the number of inner nodes present on each thread of the net proper. Consequently, the γ-th thread linking two knots (i.e., nodes with indices $1 \leq i \leq N_s^2$) together has $N_I + 1$ thread sections. At the moment of the model switching to a higher fidelity representation of the net, the mass of all knots and corner masses are recomputed so that the total mass of the net remains constant with the increased discretization. A sample net with $N_s = 11$ and $N_I = 2$ can be seen in Fig. 1.

It is possible that the length of the corner threads is not identical to the threads on the net proper itself [4, 6, 20]. As such, to ensure that the unstretched distances between the nodes' center of masses of the corner threads are the same as those of threads on the net proper, the number of nodes, including both the corner mass and inner nodes, to be added on each corner thread is based on the unstretched length of a corner thread $l_{CT,0}$ as:

$$N_{CT} = \left\lceil \frac{l_{CT,0}}{l_{min}} \right\rceil \tag{2}$$

where $l_{min} = l_{net,0}/(N_I + 1)$ given that $l_{net,0}$ is the unstretched length of each thread on the net proper. By allowing the unstretched distances between the nodes' center of masses of the corner threads to be the same as or smaller than those between the nodes of the net proper, the corner threads thus possess the same collision detection abilities as the threads on the net proper itself [20]. Corner thread nodes are given indices from $N + 1 = N_s^2 + 2N_s(N_s - 1)N_I + 1$ to $N_{tot} = N_s^2 + 2N_s(N_s - 1)N_I + 4N_{ct}$ for labelling purposes.

Newton's second law is applied to derive the equation of motion for each node present on the net:

$$m_i \mathbf{a}_i = \sum_{\xi \in \Xi_i} \pm \mathbf{T}_\xi + \sum_{s=1}^{S_i} \mathbf{F}_{ext,s,i} \tag{3}$$

In the above equation, $\mathbf{a}_i$ denotes the inertial acceleration of the i-th node, and $\mathbf{T}_\xi$ refers to the tension in the ξ-th thread section neighboring the i-th node. Meanwhile, $\mathbf{F}_{ext,s,i}$ represents each of the external forces acting on the i-th node, such forces resulting from contact between rigid bodies and gravitational forces. However, gravitational acceleration is

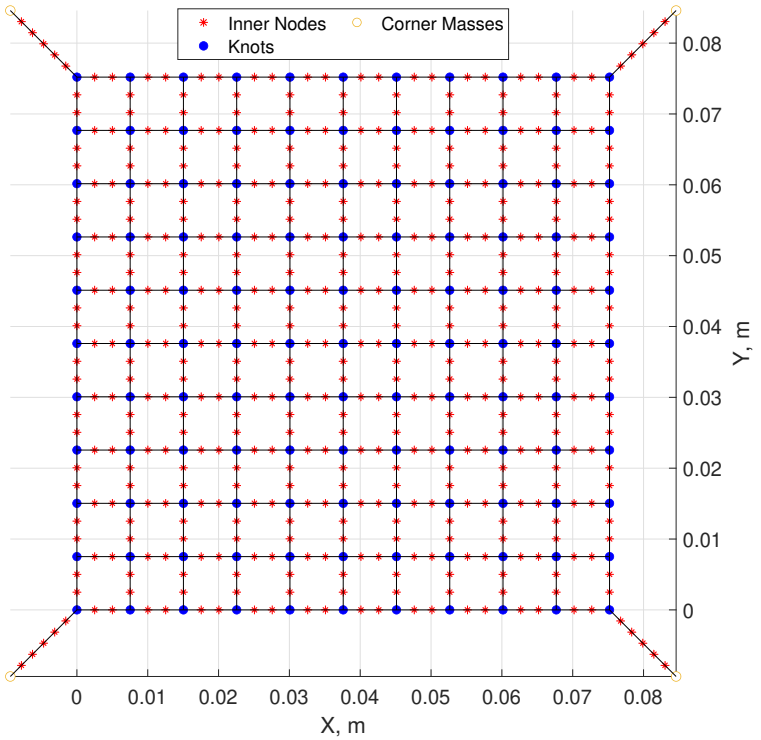

Fig. 1 Square-net layout with $N_s = 11$ and $N_I = 2$.

disregarded in this manuscript due to the relatively short time of the scenarios of interest. The tension is determined as:

$$\mathbf{T}_\xi = \begin{cases} T_\xi \mathbf{e}_\xi & \text{if } (l_\xi > l_{\xi,0}) \\ \mathbf{0} & \text{if } (l_\xi \leq l_{\xi,0}) \end{cases} \tag{4}$$

The tension magnitude T_ξ is determined using the equation $T_\xi = k_{a,\xi}(l_\xi - l_{\xi,0}) + c_{a,\xi} v_{r,\xi}$. The axial unit vector $\mathbf{e}_\xi$ represents the axial direction of the ξ-th thread section, the variables $k_{a,\xi}$ and $c_{a,\xi}$ symbolize the axial stiffness and damping coefficients of the ξ-th thread section, and l_ξ is the present thread section length, while $l_{\xi,0}$ denotes the unstretched nominal length of the thread section. Lastly, $v_{r,\xi}$ is the projected relative velocity of the nodes on each end in the axial direction of the thread section. The axial stiffness coefficient is computed as $k_{a,\xi} = EA/l_{\xi,0}$ where E and A are the Young's modulus and cross-sectional area of the thread, respectively. Meanwhile, the axial damping coefficient is computed as $c_{a,\xi} = 2\zeta k_{a,\xi}/\omega_{n1}$ where ζ and ω_{n1} are axial damping ratio and first natural frequency of the net, respectively.

Before the net is launched towards the target, it is stowed with a side length of $L_{net}\alpha$, where L_{net} is the side length of the net proper and α is the stowing ratio, which is defined as the ratio of the compacted net side length and the side length of the fully expanded net. The deployment direction in the selected coordinate system is defined as the negative Z-direction. The corner masses are assigned an initial velocity with a magnitude of v_e; their components in the X- and Y-directions are of equal magnitude and are calculated using the following expressions:

$$|v_{x,0}| = |v_{y,0}| = v_e \sin(\theta_e)/\sqrt{2} \tag{5}$$

The shooting angle, symbolized by θ_e, represents the angle between the direction of deployment and the initial velocity vector of each corner mass. The choice of equal magnitudes for $v_{x,0}$ and $v_{y,0}$ ensures that central symmetry is maintained throughout the deployment process of the net. The component of the intial velocity vector in the direction of deployment can be formulated as:

$$v_{z,0} = -v_e \cos(\theta_e) \tag{6}$$

B. Conservation of Dynamics Quantities Requirements

With the assumption that there is no gravitational acceleration present and no external forces acting on the net after launch, the total linear momentum with respect to the inertial frame of the system is a constant of the motion. Therefore, when the inner nodes are appended to the net mid-simulation, the following equation must be true:

$$\mathbf{p}(t) = \mathbf{p}(0) \tag{7}$$

where $\mathbf{p}(t) = \sum_{i=1}^{N_{tot}} m_i \mathbf{v}_i\,(t)$ is the total linear momentum of a net possessing N_{tot} nodes (including the corner masses and the nodes on corner threads if present) at time t with respect to the inertial frame. Therefore, the inner nodes must be added mid-simulation in such a way that the total linear momentum does not change. Due to the symmetric ejection of the corner masses of the net (see Eq. (5)), the total linear momentum of the net only has a Z-direction component through simulation (i.e., $\mathbf{p}(t) = p(t)\hat{\mathbf{k}}$). The work-energy principle must also hold for the system throughout the simulation:

$$T_O(t) = T_O(0) + W_{tot}(t) \tag{8}$$

where $T_O\,(t) = \frac{1}{2}\sum_{i=1}^{N_{tot}} m_i (v_i\,(t))^2$ is the total kinetic energy of the net at time t with respect to the inertial frame and $W_{tot}(t) = \int_0^t \sum_{\xi=1}^{N_{TS}} \mathbf{T}_\xi \cdot (\mathbf{v}_{1,\xi} - \mathbf{v}_{2,\xi})dt$ is the work done by the tensions of N_{TS} total thread sections of the net. During the deployment period, the second term on the right-hand side of Eq. (8) corresponds to the internal work done by the spring and damper elements, as no external forces are acting on the system while it is in that phase. Due to how all constraints are attached to the center of each node in simulation, during the deployment period, and the system's energy does not include contributions from rigid body rotations. For a more in-depth analysis of energy and momentum regarding net deployment, interested readers may consult Ref. [25].

III. Model Switching Methodology

In the following proposed methodology for mid-simulation model switching, $N_I > 0$ inner nodes are added to all net proper threads and corner threads at model switching time t_s. Before the switch, the net is set to have $N_I = 0$. In the switch, the knots and corner masses of the net maintain the same positions and velocities as before the inner nodes are introduced. To place the additional inner nodes along each γ-th thread mid-simulation, the positions of the nodes will be assigned through linear interpolation of the positions of the knots on each end of the thread:

$$\mathbf{r}_{q,\gamma}(t_s) = \mathbf{r}_{1,\gamma}(t_s) + q\frac{\mathbf{r}_{2,\gamma}(t_s) - \mathbf{r}_{1,\gamma}(t_s)}{N_I + 1} \tag{9}$$

where $\mathbf{r}_{q,\gamma}(t_s)$ is the position of the q-th inner node of the γ-th thread, $\mathbf{r}_{1,\gamma}(t_s)$ and $\mathbf{r}_{2,\gamma}(t_s)$ are the positions of the knots on each end of a thread.

Next, conserved quantities must be considered for assigning the velocity to each added inner node. First, the conservation of linear momentum must be adhered to. As such, for a given γ-th thread, the following relation must hold true:

$$\mathbf{p}_{\gamma,A}(t_s) = \mathbf{p}_{\gamma,B}(t_s) \tag{10}$$

where $\mathbf{p}_{\gamma,A}(t_s)$ and $\mathbf{p}_{\gamma,B}(t_s)$ are the total linear momentum of the γ-th thread after and before the model switching, respectively. In Vortex Studio, the instance where the inner nodes are introduced mid-simulation is at the current timestep of the numerical integration of the simulation, not at the next or previous timestep. As such, the elapsed in-simulation time between the net without the model switch and the net with the model switch is zero; therefore, the work done and impulse on the system are zero in the transition from the net without the model switch and the net with the model switching. In the case of the net before model switching with $N_I = 0$, $\mathbf{p}_{\gamma,B}(t_s)$ can be expressed as:

$$\mathbf{p}_{\gamma,B}(t_s) = \frac{m_\gamma}{2}\mathbf{v}_{1,\gamma}(t_s) + \frac{m_\gamma}{2}\mathbf{v}_{2,\gamma}(t_s) \tag{11}$$

where m_γ is the total mass of the γ-th thread. The initial assignment for the velocities assigned to each added inner node is computed as follows:

$$\mathbf{v}_{q,\gamma}(t_s) = \mathbf{v}_{1,\gamma}(t_s) + q\frac{\mathbf{v}_{2,\gamma}(t_s) - \mathbf{v}_{1,\gamma}(t_s)}{N_I + 1} \tag{12}$$

In the expression, $\mathbf{v}_{q,\gamma}(t_s) = \dot{x}_{q,\gamma}\hat{\mathbf{i}} + \dot{y}_{q,\gamma}\hat{\mathbf{j}} + \dot{z}_{q,\gamma}\hat{\mathbf{k}}$ is the velocity of the q-th inner node added mid-simulation for the γ-th thread, while $\mathbf{v}_{1,\gamma}(t_s)$ and $\mathbf{v}_{2,\gamma}(t_s)$ are the velocities of the knots on each end of a thread. This velocity choice is

equivalent to the linear interpolation of velocity between two adjacent knots. With Eq, (12), the total linear momentum of the γ-th thread after model switching $\mathbf{p}_{\gamma,A}(t_s)$ is computed as:

$$\mathbf{p}_{\gamma,A}(t_s) = \frac{m_\gamma}{2(N_I+1)}\mathbf{v}_{1,\gamma}(t_s) + \frac{m_\gamma}{2(N_I+1)}\mathbf{v}_{2,\gamma}(t_s) + \frac{m_\gamma}{(N_I+1)}\sum_{q=1}^{N_I}\mathbf{v}_{1,\gamma}(t_s) + q\frac{\mathbf{v}_{2,\gamma}(t_s) - \mathbf{v}_{1,\gamma}(t_s)}{N_I+1} \tag{13}$$

Through algebraic simplification, it can be shown that Eq. (13) is equivalent to Eq. (11). As such, the linear momentum of the γ-th thread is conserved. The process is identical for both threads on the net proper and the corner threads, except that corner threads utilize N_{CT} for the computation instead of N_I. Since the total mass of the net and the total linear momentum of each thread that constitutes the net are constant before and after the switching, the total linear momentum of the net itself is constant.

However, utilizing the conservation of linear momentum does not guarantee the conservation of kinetic energy (note that W_{tot} between before and after model switching is zero since the elapsed simulation time is zero). To correct the inner node velocities such that both total linear momentum and kinetic energy of the net are conserved, first, define the net without and with model switching at time t_s to possess kinetic energy of:

$$T_O\,(t_s) = \frac{1}{2}\sum_{i=1}^{N_{tot,B}} m_{i,B}(v_i\,(t_s))^2 = \frac{1}{2}\sum_{i=1}^{N_{tot,B}} m_{i,A}(v_i\,(t_s))^2 + \frac{1}{2}\sum_{\gamma=1}^{N_T}\sum_{q=1}^{N_I} m_{q,\gamma,new}(v_{q,\gamma,new}\,(t_s))^2 \tag{14}$$

where $N_{tot,B}$ is the total number of nodes of the net before model switching, N_T is the total number of threads of the net, $m_{q,\gamma,new}$ is the mass of the q-th added inner node of the γ-th thread, and $v_{q,\gamma,new}(t_s)$ is the magnitude of the modified velocity of the q-th inner node $\mathbf{v}_{q,\gamma,new}(t_s)$ defined as:

$$\mathbf{v}_{q,\gamma,new}(t_s) = \begin{bmatrix} c & 0 & 0 \\ 0 & c & 0 \\ 0 & 0 & 1 \end{bmatrix}\mathbf{v}_{q,\gamma}(t_s) \tag{15}$$

where the correction factor c is applied to the X- and Y-components for the modified velocity. Due to the ejection symmetry of the net, and the fact that the total linear momentum only has a component in the Z- direction, multiplying the X- and Y-components of $\mathbf{v}_{q,\gamma}(t_s)$ with c will result in a net zero change in the total linear momentum. As such, Eq. (14) can be rewritten as:

$$T_O\,(t_s) = \frac{1}{2}\sum_{i=1}^{N_{tot,B}} m_{i,B}(v_i\,(t_s))^2 = \frac{1}{2}\sum_{i=1}^{N_{tot,B}} m_{i,A}(v_i\,(t_s))^2 + \frac{1}{2}\sum_{\gamma=1}^{N_T}\sum_{q=1}^{N_I} m_{q,\gamma,new}(c^2\dot{x}_{q,\gamma}^2 + c^2\dot{y}_{q,\gamma}^2 + \dot{z}_{q,\gamma}^2) \tag{16}$$

The constant c can be solved for which yields the following expression:

$$c = \pm\sqrt{\frac{\sum_{i=1}^{N_{tot,B}}(m_{i,B} - m_{i,A})(v_i\,(t_s))^2 - \sum_{\gamma=1}^{N_T}\sum_{q=1}^{N_I} m_{q,\gamma,new}\dot{z}_{q,\gamma}^2}{\sum_{\gamma=1}^{N_T}\sum_{q=1}^{N_I} m_{q,\gamma,new}(\dot{x}_{q,\gamma}^2 + \dot{y}_{q,\gamma}^2)}} \tag{17}$$

where $m_{i,B}$ and $m_{i,A}$ are the masses of the i-th nodes before and after model switching. The value of $c = 1$ is equivalent to no modifications of X-Y components of the inner nodes velocities. At the same time, $c > 1$ and $c < 1$ are equivalent to the increased and decreased magnitude of velocity components in the X-Y directions, respectively. In most practical deployment cases, the constant c will always be a real number. In Eq. (17), the quantity $\sum_{i=1}^{N_{tot,B}}(m_{i,B} - m_{i,A})(v_i\,(t_s))^2$, which includes the energy contributions from knots and corner masses (where the majority of the net mass is distributed to), is greater than the quantity $\sum_{\gamma=1}^{N_T}\sum_{q=1}^{N_I} m_q\dot{z}_{q,\gamma}^2$ which includes the energy contributions from only the motion of the inner nodes in the Z-direction; the difference is then divided by a positive quantity $\sum_{\gamma=1}^{N_T}\sum_{q=1}^{N_I} m_{q,\gamma,new}m_q(\dot{x}_{q,\gamma}^2 + \dot{y}_{q,\gamma}^2)$, thus resulting in the term under the square-root to be positive. For the results presented in later Sections of this work, the constant c is chosen to be greater than zero as to not alter the signs of the X-Y components of the inner nodes velocities.

To account for the change in the unstretched distances between the nodes due to the addition of inner nodes along the threads, the net threads' axial stiffness and damping coefficients have to be adjusted. Based on the unstretched length of threads between knots of the net proper $l_{net,0}$, the unstretched length between inner nodes of the net proper is computed

as $l_{\xi,0} = l_{net,0}/(N_I + 1)$. Therefore, the stiffness and damping coefficients are recomputed as $k_{aA,\xi} = EA/l_{\xi,0}$ and $c_{aA,\xi} = 2\zeta k_{aA,\xi}/\omega_{n1}$, respectively. Meanwhile, the new unstretched length of thread sections on the corner threads is equal to $l_{CT,0}/(N_{CT} + 1)$ with N_{CT} determined from Eq. (2). The corner thread sections' stiffness and damping properties are determined similarly to those of the thread sections on the net proper. Modifying the stiffness and damping coefficients in such a matter ensures that the elastic potential energy stored by the γ-th thread – defined as $U_\gamma = \sum_{\xi=1}^{N_I+1} \frac{1}{2} k_{aA,\xi}(l_\xi - l_{\xi,0})^2$ – is identical before and after model switching.

IV. Results and Analysis

To demonstrate the ability of the methodology proposed in Section III to append inner nodes mid-deployment at varying switching times and for varying net geometries, two net designs with two different amounts of N_I added will be studied within this section. The nets within this section initially possess $N_I = 0$ inner nodes, and $N_I > 0$ inner nodes are added mid-deployment. For each design, the effects of two different model switching times during deployment will be studied. These comparisons will provide an understanding of the impact of the model-switching strategy in terms of both computational time and its impact on the deployment dynamics of nets after the switching has been implemented. The deployment simulations utilizing both net designs in Vortex Studio utilize integration timestep of 10^{-6} s.

In the first considered net design, the net is taken to have the physical dimensions and corner masses mass identical to that of the net considered in prior work by Boonrath and Botta [20]. However, the perimeter threads of the net have the same physical properties as the interior threads of the net proper as to make the net proper thread properties homogeneous for design simplification purpose. The physical properties of Net Design 1 can be seen in Table 1. The net is initially compacted with $\alpha = 0.094$ and launched in the direction of the negative Z-axis via the ejection of the corner masses with $v_e = 1.8$ m/s and $\theta_e = 25°$. Following the values presented in Table 1, it is chosen that $N_I = 8$ will be added for the net mid-deployment. The simulation end-time is determined to be $t = 0.9$ s, as it is when the net reaches an almost fully flattened-out configuration in prior work [20].

Table 1 Physical Properties of Net Design 1

Parameter	Value
Net Side Length L_{net}, m	0.8
Net Mesh Length $l_{net,0}$, m	0.08
Net Proper Thread Radius r_{net}, m	0.0005
Net Proper and Corner Thread Density ρ, kg/m^3	1390
Net Proper and Corner Thread Young's Modulus E, GPa	0.4460
Net Proper and Corner Thread Damping Ratio ζ,-	0.106
Corner Thread Length $l_{CT,0}$, m	0.14142
Corner Thread Radius r_{CT}, m	0.0015
Corner Mass Mass m_{CM}, kg	0.03

In the second net design considered, the net is taken to have all physical properties and dimensions to be identical to those of the net considered within work by Botta et al. [8, 25] with $L_{net} = 5$ m and $N_s = 6$. The physical properties of Net Design 2 can be seen in Table 2. The net is initially compacted with $\alpha = 0.25$ and launched in the direction of the negative Z-axis via the ejection of the corner masses with $v_e = 2.5$ m/s and $\theta_e = 36.87°$. Following the values presented in Table 2 with $N_s = 6$, it is chosen that $N_I = 2$ nodes per thread will be added for the net mid-deployment. The simulation end-time is determined to be $t = 3.0$ s, as it is when the net reaches an almost fully flattened out configuration in prior work [8].

A. Demonstration of Conservation Properties for Varying Net Geometry and Switching Time

Figure 2 displays the conservation of total linear momentum using the described methodology for model switching applied to Net Design 1 with switching times of $t_s = 0.75$ s and $t_s = 0.50$ s. The components of the total linear momentum vectors (Fig. 2(a) - (c)) and the total linear momentum magnitudes (Fig. 2(d)) are observed to be constant throughout both model switching simulations. As expected from the net deployment's symmetry, the total linear momentum components in the X- and Y-directions are zero (See Fig. 2(a) and 2(b)). This is true for both entire nets

Table 2 Physical Properties of Net Design 2

Parameter	Value
Net Side Length L_{net}, m	5
Net Mesh Length $l_{net,0}$, m	1
Net Proper Thread Radius r_{net}, m	0.001
Net Proper and Corner Thread Density ρ, kg/m^3	1390
Net Proper and Corner Thread Young's Modulus E, GPa	70
Net Proper and Corner Thread Damping Ratio ζ,-	0.106
Corner Thread Length $l_{CT,0}$, m	1.4142
Corner Thread Radius r_{CT}, m	0.002
Corner Mass Mass m_{CM}, kg	0.5

and when the components are separated into the contributions from the knots and corner masses and inner nodes. For both switching times, it can be observed in Fig. 2(c) that the Z-components of the total linear momentum of the knots and corner masses decreases after the instances of switching. This is explained by the fact that, due to the increased discretization of the net through the addition of the inner nodes, the combined mass of the knots and corner masses are reduced. With the methodology described in Section III, the knots and corner masses velocities are maintained when the model switching occurs. As such, Z- components of the total linear momentum, and thus also the overall magnitude of the linear momentum of the knots and corner masses, decreases as seen in Fig. 2(d). These reductions are counteracted by inner nodes' contributions to the nets' total linear momentum such that the total quantities are the same as the net before the model switching.

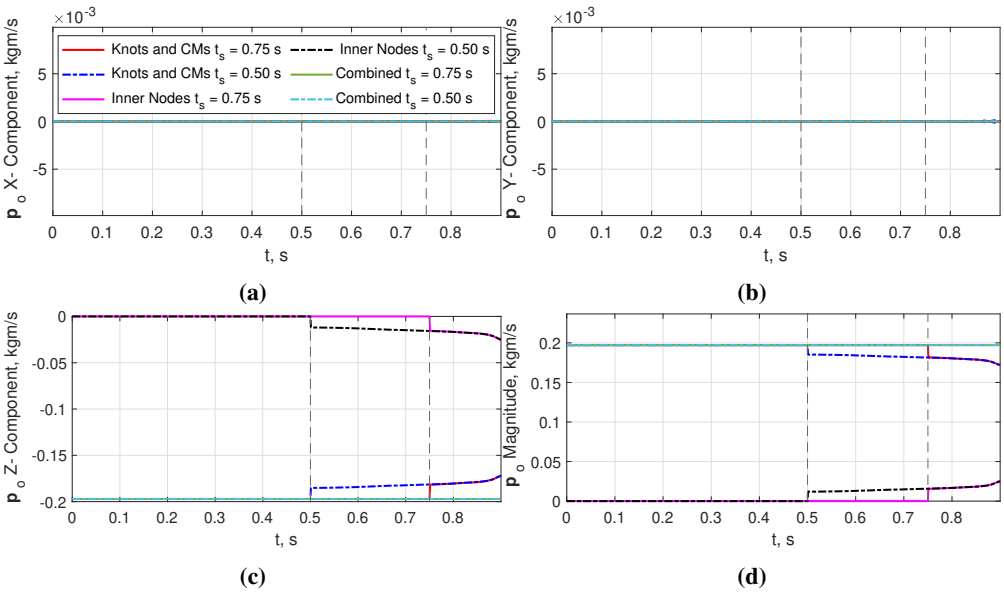

Fig. 2 Conservation in a) X-component, b) Y-component, c) Z-component, and d) the magnitude of total linear momentum for Net Design 1.

It can also be seen from Fig. 3 that the work-energy principle is adhered to with switching times of $t_s = 0.75$ s and $t_s = 0.50$ s, respectively. For both switching times, there is no change in the sums of kinetic energies and the work done over time of the systems. Due to the damping properties within the constraints that link the nodes together, the nets lost kinetic energy over time via internal work W^{int}. As such, the summation of T_O and W^{int} results in a constant value of 0.1958 J throughout the simulation. The correction factors are $c = 1.08567$ and $c = 1.04377$ for $t_s = 0.75$ s and $t_s = 0.50$ s, respectively. Both c values indicate that for Net Design 1, the required corrections to the inner nodes'

initially determined velocities are minimal overall. The constant c for $t_s = 0.75$ s is slightly larger than that of $t_s = 0.50$ s, implying that greater corrections are required for the inner node's X- and Y-direction velocity components as more time passes after the initial net launch. The methodology described in Section III demonstrates satisfactory performance through its ability to both conserve total linear momentum and adhere to the work-energy principle for Net Design 1.

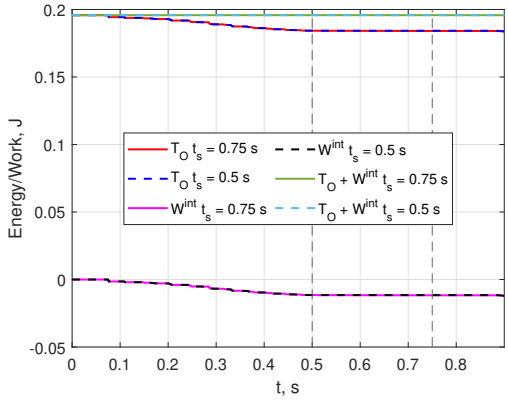

Fig. 3 Work and kinetic energy of model switching nets with Net Design 1.

Figure 4 displays the conservation of total linear momentum using the described methodology for model switching applied to Net Design 2 with switching times of $t_s = 2.70$ s and $t_s = 2.25$ s. Same as with Net Design 1, the components of the total linear momentum vectors (Fig. 4(a) - (c)) and the total linear momentum magnitudes (Fig. 4(d)) are observed to be constant for the considered switching times. It is noted that there are minor fluctuations – which can be attributed to the numerical integration error – in the linear momentum magnitudes of the knots and inner nodes in the X- and Y-directions toward the end of the simulation, as can be seen in Fig. 4(a) and 4(b). However, the total values of the linear momentum components in X- and Y-directions considering all nodes (corresponding to solid green and dashed cyan lines in Fig. 4) are still zero. It is again observed from Fig. 4(c) and Fig. 4(d) that the Z-components magnitudes and magnitudes of total linear momentum of the knots and corner masses reduce in value after the instance of switching due to the same reason as that of Net Design 1. As before, the decreases are counteracted by the linear momentum components of the added inner nodes. Both Fig. 4 and Fig. 2 thus show that the proposed model switching methodology conserves the total linear momentum of the nets of varying sizes using varying switching times.

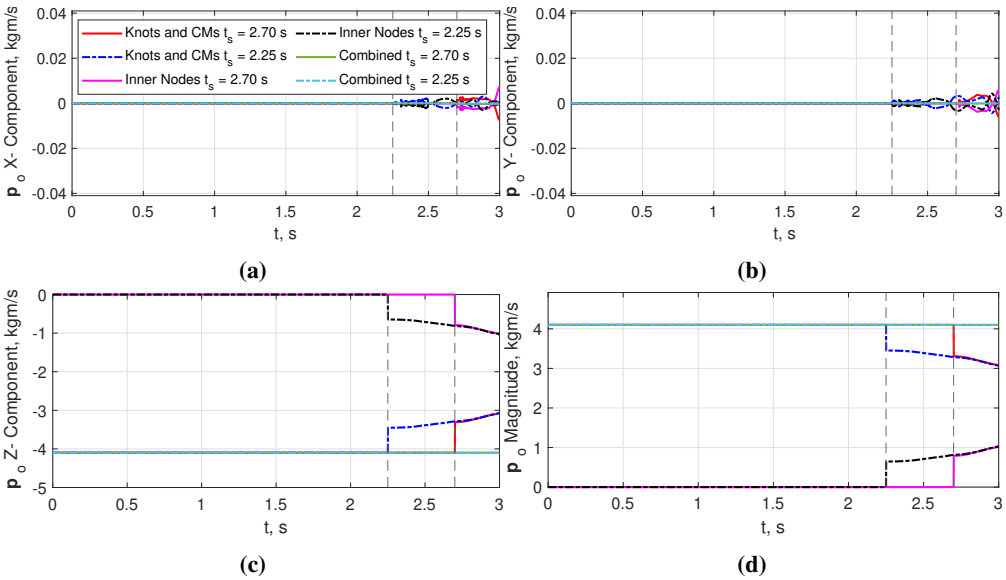

Fig. 4 Conservation in a) X-component, b) Y-component, c) Z-component, and d) the magnitude of total linear momentum for Net Design 2.

Figure 5 illustrates very similar trends to those found in Fig. 3. For both $t_s = 2.70$ s and $t_s = 2.25$ s, no change in the sum of kinetic energies and the negative of work done on the systems are observed as seen in Fig. 5; the sum remains at 6.41 J throughout both simulations. The correction factors are $c = 1.21146$ and $c = 1.08568$ for $t_s = 2.70$ s and $t_s = 2.25$ s, respectively; both values are larger than the counterpart values of Net Design 1. Same as with Net Design 1, the constant c for the later switching case with $t_s = 2.70$ s is larger than that of the earlier switching case of $t_s = 2.25$ s; these values reinforce the finding that greater corrections are required for the X- and Y-direction velocity components of inner nodes as more time passes after the initial net launch. More significant kinetic energy losses through internal work, of 1.32 J. are observed for Net Design 2 (see Fig. 5) compared to kinetic energy losses through internal work, of 0.12 J, in Net Design 1 (see Fig. 3). This is due to a number of factors, including an increased thread radius and consequently larger stiffness and damping coefficients, a greater initial kinetic energy, and a longer simulation time for Net Design 2 compared to Net Design 1. Overall, both Fig. 4 and Fig. 2 show that the proposed methodology allows the model switching of nets of varying sizes using varying switching times to adhere to the work-energy principle.

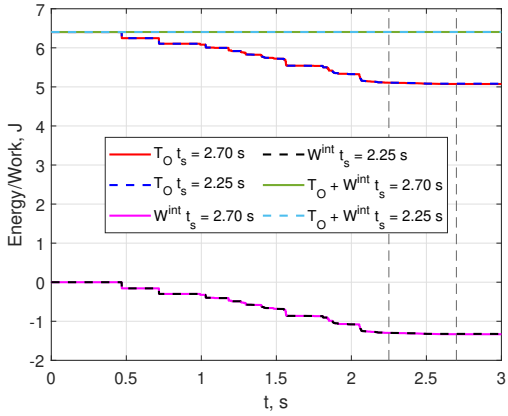

Fig. 5 Work and kinetic energy of model switching nets with Net Design 2.

B. Quantitative and Qualitative Comparison Between Model Switch and No Model Switch Nets

For model switching to be viable within simulations, nets after model switching need to maintain similar dynamics to nets without model switching launched using identical initial conditions. Utilizing the same net designs considered in Section IV.A, nets with model switching mid-deployment and without model switching (i.e., $N_I = 0$ throughout simulation) will be compared in this Section. The comparisons are both performed quantitatively through the usage of the Root Mean Square Error (RMSE) in the positions and velocities of the nets over time and quantitatively through visual comparison of the shapes of the nets at the end of the deployment.

The Root Mean Square Error (RMSE) values over time for the simulations are computed as:

$$RMSE_{pos,tot}(t) = \sqrt{\sum_{i=1}^{N_{tot,B}} \frac{\left(x_i^S(t) - x_i^{NS}(t)\right)^2 + \left(y_i^S(t) - y_i^{NS}(t)\right)^2 + \left(z_i^S(t) - z_i^{NS}(t)\right)^2}{N_{tot,B}}} \tag{18}$$

$$RMSE_{vel,tot}(t) = \sqrt{\sum_{i=1}^{N_{tot,B}} \frac{\left(\dot{x}_i^S(t) - \dot{x}_i^{NS}(t)\right)^2 + \left(\dot{y}_i^S(t) - \dot{y}_i^{NS}(t)\right)^2 + \left(\dot{z}_i^S(t) - \dot{z}_i^{NS}(t)\right)^2}{N_{tot,B}}} \tag{19}$$

where $N_{tot,B}$ is the total number of knots and corner masses (which is constant before and after model switching), $(.)^{NS}$ are quantities that correspond to the net without model switching, and $(.)^S$ are quantities that correspond to the net with model switching. As the nets without model switching do not have inner nodes along the threads of the net proper and corner threads, the RMSE values will only compare the positions and velocities over time for the knots and corner masses (which are present both with and without model switching).

Figure 6 compares Net Design 1 without model switching and with model switching at $t_s = 0.75$ s and $t_s = 0.50$ s. As expected, due to identical initial conditions given to the nets, the positions and velocities RMSE of the nets are zero until the model switching times are reached. Both Fig. 6(a) and 6(b) show that the positions RMSE values are overall

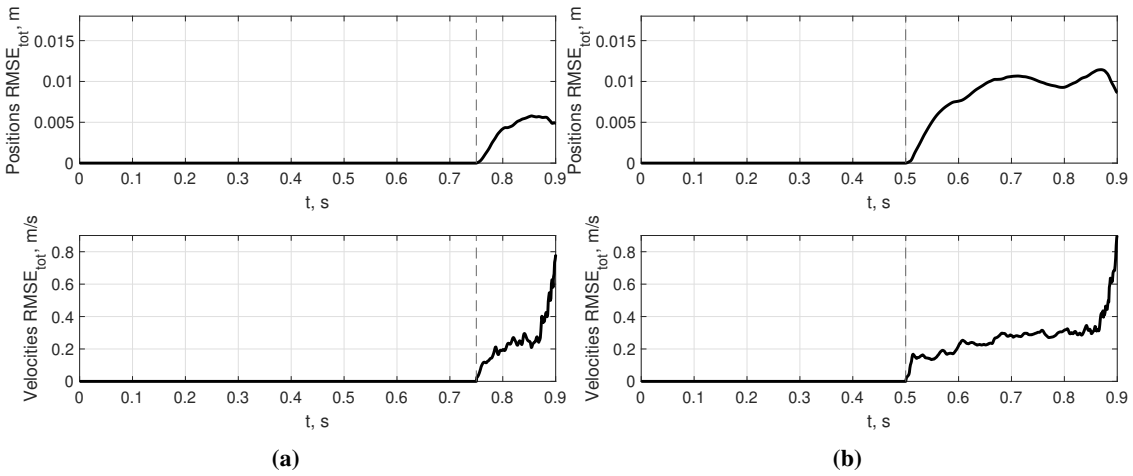

Fig. 6 RMSE between net with and without model switch in knots and corner masses positions and velocities for Net Design 1 at a) $t_s = 0.75$ s and b) $t_s = 0.50$ s.

relatively low over time, never exceeding 0.006 m and 0.012 m for model switching at $t_s = 0.75$ s and $t_s = 0.50$ s, respectively. Compared to the net side length of $L_{net} = 0.8$ m and distances the nets travel for the deployment of approx. 1.5 m, these values are relatively small. This indicates that introducing inner nodes mid-simulation results in minor changes in the positions of the knots and corner masses over time. As can be seen in the lower plots of Fig. 6(a) and 6(b), the RMSE in the velocities of the nets are still small but more considerable, especially at the end of the simulations where there are sharp increases in values to approx. 0.8 and 0.9 m/s for $t_s = 0.75$ s and $t_s = 0.50$ s, respectively.

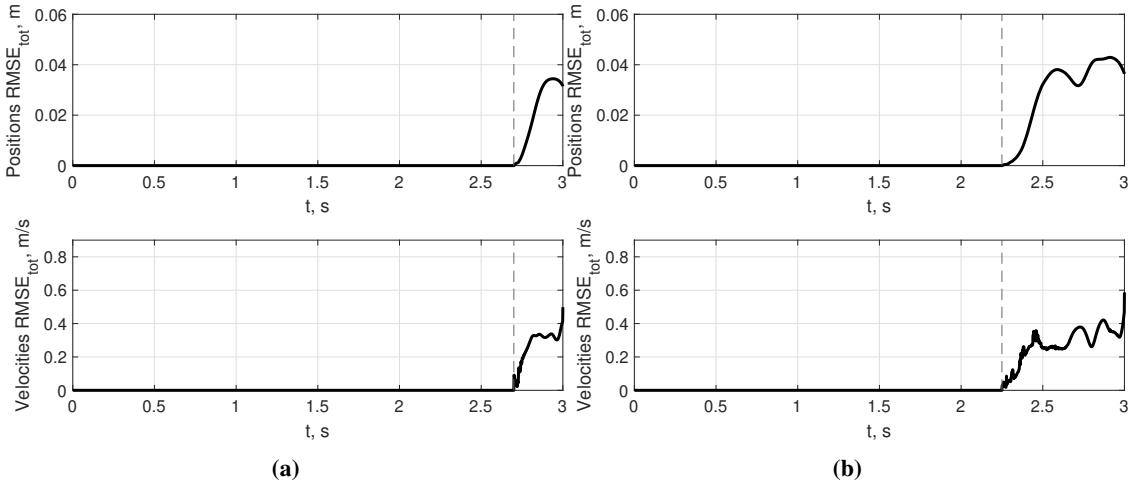

Fig. 7 RMSE between net with and without model switch in knots and corner masses positions and velocities for Net Design 2 at a) $t_s = 2.70$ s and b) $t_s = 2.25$ s.

The trends observed in Fig. 7 are very similar to those found in Fig. 6. Figure 7 compares Net Design 2 without model switching and with model switching at $t_s = 2.7$ s and $t_s = 2.25$ s. Both Fig. 7(a) and 7(b) show that the position RMSE values are overall relatively low over time, never exceeding approx. 0.035 m and 0.045 m for model switching at $t_s = 2.7$ s and $t_s = 2.25$ s, respectively. Compared to the net side length of $L_{net} = 5$ m and distances the nets travel for the deployment of approx. 5 m, these values are relatively small. It is noted that even though the corner masses of Net Design 2 are given greater ejection speeds compared to Net Design 1, the RMSE in the velocities between model switching and no model switching nets (see lower plots of Fig. 7(a) and 7(b)) are lower than the counterpart plots of Net Design 1 (see lower plots of Fig. 6(a) and 6(b)). For Net Design 1, the greatest velocities RMSE is observed in Fig. 6(b) at approx. 0.9 m/s while the greatest velocities RMSE for Net Design 2 is observed in Fig. 6(b) at approx. 0.6 m/s.

This can be explained through the fewer nodes in Net Design 2, thus resulting in less propagation of differences in the deployment dynamics over time.

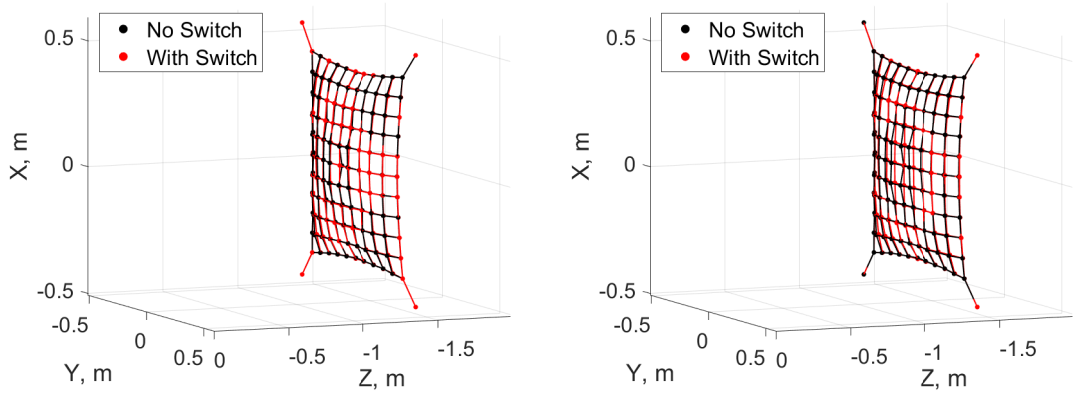

(a) $t = 0.9$ **s** **(b)** $t = 0.9$ **s**

Fig. 8 Shape comparison between net with and without model switch with Net Design 1 at a) $t_s = 0.75$ **s and b)** $t_s = 0.50$ **s.**

In addition to the quantitative comparison done by the RMSE values, Fig. 8(a) and (b) plot the geometric shapes of Net Design 1 at the end of deployment ($t = 0.9$ s) for model switching times of $t_s = 0.75$ s and $t_s = 0.5$ s, respectively. As expected from the RMSE values displayed in Fig. 6, the shapes of the nets with model switching are very similar to those of the net without model switching. The positions of corner masses and knots located on the perimeter of the nets are almost identical between nets with and without model switching. However, it can be noticed that the central knots of the net with model switching in Fig. 8(b) deviate from the central knots of the net without model switching more than the central knots of the net with model switching in Fig. 8(a). This difference can be explained by how, due to the earlier switching time, the dynamics of the net is given more time to deviate from the no-switching case in Fig. 8(b) compared to Fig. 8(a). Overall, Fig. 8(a) and (b) demonstrate that the effects of model switching time on the shapes of the nets at the end of deployment are minimal.

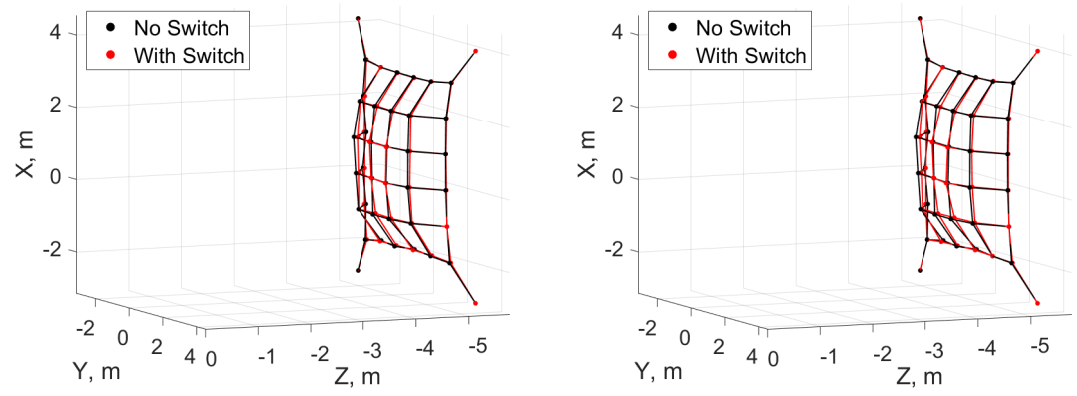

(a) $t = 3.0$ **s** **(b)** $t = 3.0$ **s**

Fig. 9 Shape comparison between net with and without model switch with Net Design 2 at a) $t_s = 2.70$ **s and b)** $t_s = 2.25$ **s.**

Figures 9(a) and (b) plot the geometric shapes of Net Design 2 at the end of deployment ($t = 3.0$ s) for model switching times of $t_s = 2.7$ s and $t_s = 2.25$ s, respectively. Same as in the case of Net Design 1, the shapes of the model switch nets are very similar to those of the net without model switching, in agreement with Fig. 7. The nets of Net

Design 2 also have positions of corner masses and knots located on the perimeter of the nets that are nearly identical between nets with and without model switching. Unlike with Net Design 1, the central knots of Net Design 2 nets with model switching in Fig. 9(b) deviate from the central knots of the net without model switching in a very similar manner to the central knots of the net with model switching in Fig. 9(a). The lower deviation can be explained by the number of nodes present as knots and added inner nodes, resulting in less propagation of differences in the deployment dynamics. Both Net Design 1 and Net Design 2 show that model switching has minor effects on the end-of-deployment net shapes regardless of the choice of appended inner nodes mid-simulation and the geometries of the nets, thus indicating that the proposed methodology is capable of maintaining the desired net shapes.

C. Capture of an Envisat Satellite Model with Model Switch and No Model Switch Nets

To demonstrate the ability of a net with model switching to capture a target with thin geometries, the net with $N_s = 11$ studied in the previous sections is employed to capture a scaled-down model of the Envisat satellite using $N_I = 20$. This scenario is identical – except for the lack of residual angular velocity and gravity – to that which was studied by Boonrath and Botta for the validation of the simulator [20]. The capture performance of the net with model switching will be compared to that of the net without model switching. As the chosen target possesses thin panels that require the usage of $N_I = 20$ to enable the net to wrap around it [20], the dynamics simulation can be expedited through the use of model switching. Unlike in previous sections where the nets without model switching possess $N_I = 0$ throughout simulations, in this capture scenario, the net without model switching needs to have $N_I = 20$ throughout the simulation to enable it to capture the Envisat model.

Figure 10 provides snapshots for simulations with model switching at $t_s = 0.75$ s (Fig. 10(a), 10(c), and 10(e)) with no model switching (Fig. 10(b), 10(d), and 10(f)). In the scenario, the top-left corner of the Envisat satellite model fuselage, as viewed from the inertial reference frame, is located at $X = -0.05$ m, $Y = 0.1286$ m, and $Z = -1.5$ m. On a computer with Intel(R) Core(TM) i9-9900K CPU @ 3.60GHz processor and GeForce RTX 2070 graphics card, the simulation with model switching took 245.5 min to integrate, while without model switching – with $N_I = 20$ present since the beginning of the simulation – the simulation took 592 min to integrate; this is equivalent to approx. 2.45 times greater computational time. From Fig. 10(a) and Fig. 10(b) – which are taken 0.1 s after the model switching – it can be seen that both nets possess similar but not identical shapes. This can be attributed to the correction factor c, which results in the X-Y components of the inner nodes' velocities being different between the two models. As both snapshots are taken near the end of the deployment, both nets are at almost fully expanded configurations. Meanwhile, Fig. 10(c) and Fig. 10(d) show the nets halfway through their processes of wrapping around the target. It can be seen that the two nets are very similar to each other in their shapes mid-wrapping. The threads of both nets are seen to contact the thin panel on the lower-left side of the target, the thin panel on top of the target fuselage, and the thin rod on the lower-right right side of the target. Lastly, in Fig. 10(e) and Fig. 10(f) – which are taken at the end of the capture simulation – it can be seen that both nets are successful in capturing the Envisat model in simulation, as both models are observed to have fully wrapped around the thin panel on the lower-left side of the target. Overall, Fig. 10 indicates that both nets wrap around the target at similar rates and finish the first wrapping period at similar times. These findings show that the model switching net can replicate the capture performance of a net with $N_I = 20$ present since the beginning of the simulation while having much lower computational cost.

To quantitatively compare the capture performance of the two nets, the Capture Quality Index (CQI) is employed within this work. Proposed by Barnes and Botta [26], the CQI is computed as:

$$J = 0.1\frac{|V_n - V_t|}{V_t} + 0.1\frac{|S_n - S_t|}{S_t} + 0.8\frac{|q_n|}{L_c} \tag{20}$$

where V_n and V_t are the convex hull volume of the net and of the target, respectively, S_n and S_t are the surface area of the convex hull of the net and of the target, respectively, q_n is the distance between the centroids of the net and of the target, and L_c is the shortest distance between the centroid of the target and its surface. Same as in previous work involving the Envisat model by Boonrath and Botta [20], the convex hull volume of the target was used to compute the CQI by inputting the coordinates of the points on the surface of the target into the convhulln() MATLAB function. The value of J over time must converge to a small constant value to indicate that the capture of the target is successful [26]. As seen from both the experimental and simulated nets studied by Boonrath and Botta [20], the CQI values converge to between 3 and 3.5 for successful wrapping of the Envisat model.

Figure 11 showcases the CQI value over time for nets with and without model switching. The two nets possess similar CQI values throughout the deployment and capture phases (i.e., before and after $t = 0.9$ s). The trends of the

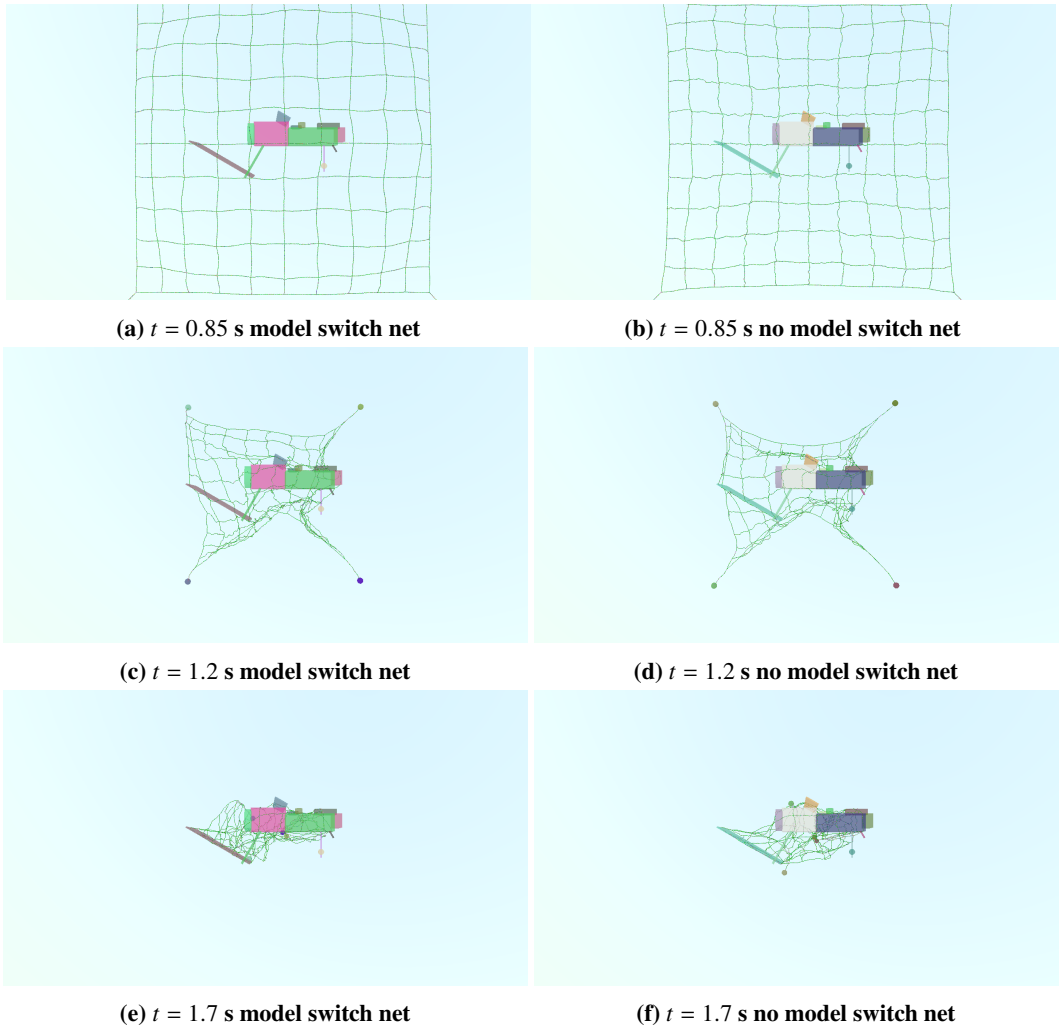

(a) $t = 0.85$ **s model switch net** **(b)** $t = 0.85$ **s no model switch net**

(c) $t = 1.2$ **s model switch net** **(d)** $t = 1.2$ **s no model switch net**

(e) $t = 1.7$ **s model switch net** **(f)** $t = 1.7$ **s no model switch net**

Fig. 10 Snapshots of the capture deployment and capture of the Envisat mockup model for a net with and without model switching.

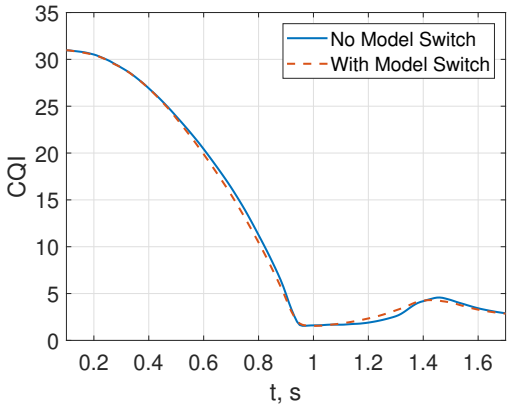

Fig. 11 CQI vs. Time for a net with and without model switching for capture of the Envisat mockup.

CQI observed over time are similar to those of the nets studied by Boonrath and Botta [20]. After $t = 0.9$ s, the CQI values gradually rise until a maximum value of the CQIs of approx. 5 are achieved at $t = 1.45$ s. Then, both CQI values

gradually decrease and settle at approx. 3 at the end of the simulation. The CQI values of the nets at the end of the simulation match well with the values corresponding to successful captures observed by Boonrath and Botta [20]. This is to be expected, as the snapshots in Fig. 10 from the Vortex-Studio-based simulator show successful wrappings of the target by the net. Therefore, the CQI quantitatively demonstrates that the net with model switching is capable of its designed capture task.

V. Conclusion

This work introduced a methodology to alter the lumped-parameter modeling for nets mid-simulation. A systematic approach to assign positions and velocities of inner nodes appended along the threads of nets is detailed, along with the computation process of thread section stiffness and damping properties. The introduced methodology can conserve total linear momentum and uphold the work-energy principle of nets mid-deployment. The nets studied within this work possess low position and velocity RMSE values – while having very similar shapes at the end of deployment – when models with and without model switching are compared. As confirmed graphically via simulation snapshots and CQI values over time, the net with model switching can capture a scaled-down model of the Envisat satellite, which has multiple thin geometries and requires many inner nodes to be utilized. Compared to the no model switching case, the capture simulation of the Envisat model is approx. 2.45 times faster with the model switching, resulting in a significant decrease in computational time. As such, mid-deployment model switching is a viable method to speed up the capture simulations in which a high number of inner nodes are required to be present.

VI. Acknowledgments

The authors thank Cailean T. Woods for creating the initial model-switching framework within Vortex Studio. The authors thank CM Labs Simulations for providing Vortex Studio simulation platform licenses. This work is supported under the CMMI Award numbered 2128578 from the National Science Foundation (NSF). The author's opinions, findings, conclusions, or recommendations expressed in this material do not necessarily reflect the views of the National Science Foundation.

References

[1] Anz-Meador, P., and Liou, J.-C., "Analysis and Consequences of the Iridium 33-Cosmos 2251 Collision," *38th COSPAR Scientific Assembly*, Bremen, Germany, July 2010.

[2] Ledkov, A., and Aslanov, V., "Review of contact and contactless active space debris removal approaches," *Progress in Aerospace Sciences*, Vol. 134, 2022, p. 100858. https://doi.org/10.1016/j.paerosci.2022.100858.

[3] Bombelli, A., "Multidisciplinary design of a net-based device for space debris active removal," Master's thesis, Politecnico di Milano, Milan, Italy, 2012.

[4] Botta, E. M., "Deployment and Capture Dynamics of Tether-Nets for Active Space Debris Removal," Ph.D. thesis, McGill University, Montreal, Québec, 2017.

[5] Shan, M., Guo, J., and Gill, E., "A Review and comparison of active space debris capturing and removal methods," *Progress in Aerospace Sciences*, Vol. 80, 2015, pp. 18–32. https://doi.org/10.1016/j.paerosci.2015.11.001.

[6] Benvenuto, R., Salvi, S., and Lavagna, M., "Dynamics analysis and GNC design of flexible systems for space debris active removal," *Acta Astronautica*, Vol. 110, 2015, pp. 247–265. https://doi.org/10.1016/j.actaastro.2015.01.014.

[7] Medina, A., Cercós, L., Stefanescu, R. M., Benvenuto, R., Pesce, V., Marcon, M., Lavagna, M., González, I., López, N. R., and Wormnes, K., "Validation results of satellite mock-up capturing experiment using nets," *Acta Astronautica*, Vol. 134, 2017, pp. 314–332. https://doi.org/10.1016/j.actaastro.2017.02.019.

[8] Botta, E. M., Sharf, I., Misra, A. K., and Teichmann, M., "On the simulation of tether-nets for space debris capture with Vortex Dynamics," *Acta Astronautica*, Vol. 123, 2016, pp. 91–102. https://doi.org/10.1016/j.actaastro.2016.02.012.

[9] Botta, E. M., Sharf, I., and Misra, A. K., "Simulation of tether-nets for capture of space debris and small asteroids," *Acta Astronautica*, Vol. 155, 2019, pp. 448–461. https://doi.org/10.1016/j.actaastro.2018.07.046.

[10] Shan, M., Guo, J., Gill, E., and Gołębiowski, W., "Validation of Space Net Deployment Modeling Methods Using Parabolic Flight Experiment," *Journal of Guidance, Control, and Dynamics*, Vol. 40, No. 12, 2017, pp. 3319–3327. https://doi.org/10.2514/1.G002761.

[11] Shan, M., Guo, J., and Gill, E., "Contact dynamic models of space debris capturing using a net," *Acta Astronautica*, Vol. 158, 2019, pp. 198–205. https://doi.org/10.1016/j.actaastro.2017.12.009.

[12] Si, J., Pang, Z., Du, Z., and Cheng, C., "Dynamics modeling and simulation of self-collision of tether-net for space debris removal," *Advances in Space Research*, Vol. 64, 2019, pp. 1675–1687. https://doi.org/10.1016/j.asr.2019.08.006.

[13] Zhang, G., Zhang, Q., Feng, Z., Chen, Q., and Yang, T., "A simplified model for fast analysis of the deployment dynamics of tethered-net in space," *Advances in Space Research*, Vol. 68, No. 4, 2021, pp. 1960–1974. https://doi.org/10.1016/j.asr.2021.04.032.

[14] Shan, M., and Shi, L., "Analytical method for net deployment dynamics modeling and its experimental validation," *Acta Astronautica*, Vol. 200, 2022, pp. 494–505. https://doi.org/10.1016/j.actaastro.2022.08.041.

[15] Lavagna, M., Armellin, R., Bombelli, A., Benvenuto, R., and Carta, R., "Debris removal mechanism based on tethered nets," *11th International Symposium on Artificial Intelligence, Robotics and Automation in Space (i-SAIRAS 2012)*, Turin, Italy, September 2012.

[16] Wormnes, K., Jong, J. H. d., Krag, H., and Visentin, G., "Throw-nets and Tethers for Robust Space Debris Capture," *Proceedings of the 64th International Astronautical Congress, IAC*, Beijing, China, September 2013.

[17] Chen, Q., and Yang, L., "On dynamics of casting a net structure of flexible cables on orbit," *Proceedings of the 60th International Astronautical Congress, IAC*, Daejeon, Republic of Korea, October 2009.

[18] Liu, H., Zhang, Q., Yang, L., and Zhu, Y., "Modeling and simulation of deployment dynamics of space webs," *Proceedings of the 64th International Astronautical Congress, IAC*, Beijing, China, September 2013.

[19] Shan, M., Guo, J., and Gill, E., "Deployment dynamics of tethered-net for space debris removal," *Acta Astronautica*, Vol. 132, 2017, pp. 293–302. https://doi.org/10.1016/j.actaastro.2017.01.001.

[20] Boonrath, A., and Botta, E. M., "Validation of Models for Net Deployment and Capture Simulation with Experimental Data," *Journal of spacecraft and rockets*, 2023, pp. 1–19.

[21] Huang, W., He, D., Li, Y., Zhang, D., Zou, H., Liu, H., Yang, W., Qin, L., and Fei, Q., "Nonlinear dynamic modeling of a tether-net system for space debris capture," *Nonlinear Dynamics*, Vol. 110, No. 3, 2022, pp. 2297–2315. https://doi.org/10.1007/s11071-022-07718-7.

[22] Hou, Y., Liu, C., Hu, H., Yang, W., and Shi, J., "Dynamic computation of a tether-net system capturing a space target via discrete elastic rods and an energy-conserving integrator," *Acta Astronautica*, Vol. 186, 2021, pp. 118–134. https://doi.org/10.1016/j.actaastro.2021.05.029.

[23] Huang, W., Zou, H., Liu, H., Yang, W., Gao, J., and Liu, Z., "Contact dynamic analysis of tether-net system for space debris capture using incremental potential formulation," *Advances in Space Research*, 2023. https://doi.org/10.1016/j.asr.2023.05.054.

[24] Guang, Z., and Jing-rui, Z., "Space Tether Net System for Debris Capture and Removal," *2012 4th International Conference on Intelligent Human-Machine Systems and Cybernetics*, Vol. 1, 2012, pp. 257–261. https://doi.org/10.1109/IHMSC.2012.71.

[25] Botta, E. M., Sharf, I., and Misra, A. K., "Energy and momentum analysis of the deployment dynamics of nets in space," *Acta Astronautica*, Vol. 140, 2017, pp. 554–564. https://doi.org/10.1016/j.actaastro.2017.09.003.

[26] Barnes, C. M., and Botta, E. M., "A quality index for net-based capture of space debris," *Acta Astronautica*, Vol. 176, 2020, pp. 455–463. https://doi.org/10.1016/j.actaastro.2020.06.044.